Isothermal dynamics of channeled viscoplastic lava flows and new methods for estimating lava rheology

J. C. Robertson[1] and R. C. Kerr[1]

Received 27 May 2011; revised 1 November 2011; accepted 4 November 2011; published 11 January 2012.

[1] This study analyses the influence of a viscoplastic lava rheology on the dynamics of lava flows. Using a multigrid-based augmented Lagrangian scheme, we find a numerical solution for the flow of a Bingham fluid in a rectangular channel. The numerical results show that an internal viscoplastic rheology significantly modifies the velocity distribution within a lava flow through the development of plug regions whose size is determined by the magnitude of the yield strength. The flow rate, maximum surface velocity and central plug dimensions are determined as functions of the channel geometry and fluid rheology, and comparisons between these and several limiting analytical solutions confirm the accuracy of the numerical method used. The results are also compared to incorrect models which have been proposed previously in the literature. Several algorithms that extend the results to different sets of measured initial parameters are outlined; these calculate: (1) the flow depth when the fluid rheology (viscosity and yield strength) and downstream flow rate are given, (2) the flow depth when the fluid rheology and maximum downstream surface velocity are given, (3) the flow rate and fluid rheology when the flow depth, maximum surface velocity and surface plug width are given, and (4) the flow depth and rheology when the flow rate, maximum surface velocity and surface plug width are given. The use of these algorithms is demonstrated by considering the dynamics of a typical lava flow on Mount Etna, using measured rheological parameters and field observations.

Citation: Robertson, J. C., and R. C. Kerr (2012), Isothermal dynamics of channeled viscoplastic lava flows and new methods for estimating lava rheology, *J. Geophys. Res.*, *117*, B01202, doi:10.1029/2011JB008550.

1. Introduction

[2] A clear understanding of the interaction of lava rheology and flow dynamics forms a crucial basis for the interpretation of lava flow morphology, the design of predictive models for lava flow emplacement and the development of mitigation strategies to minimize flow hazards to people or property (Figure 1). A fully molten lava has a purely Newtonian rheology [*Gonnermann and Manga*, 2007]. However progressive crystallization of lava driven by cooling and degassing can generate a touching network of crystals. This network can bear a stress in addition to the viscous response of the melt fraction of the lava [e.g., *Pinkerton and Sparks*, 1978; *Kerr and Lister*, 1991; *Pinkerton and Norton*, 1995; *Hoover et al.*, 2001; *Cimarelli et al.*, 2011], and the lava will only flow when the shear stress induced by the weight of the fluid exceeds this yield strength.

[3] The dynamics of a given flow may be significantly affected by fluid rheology. As a qualitative example, stirring and internal convection are important processes by which the lava can transfer the effects of surficial heat loss throughout the flow [*Griffiths*, 2000; *Griffiths et al.*, 2003; *Cashman et al.*, 2006]. The introduction of an internal yield strength limits the regions in which shear and convection can occur and reduces the rate of heat loss from the flow surface. Similarly, adding a yield strength to a lava flow will result in a thicker flow, all else being equal. Thus viscoplastic flows may more easily overcome topographic obstacles in their path. Isothermal flows are a good starting point to examine some of these effects; if studied carefully they form a useful basis for further study of the more complicated dynamics of cooling and solidification in viscoplastic flows.

[4] In this study, we consider the isothermal, steady flow of a viscoplastic fluid in a channel of constant rectangular cross-section (see Figure 2). The addition of a yield strength to the rheology of a fluid complicates the equations governing its dynamics. Analytic solutions for isothermal viscoplastic fluid flows exist only for some simple flow configurations; essentially one dimensional or axisymmetric shear flows (e.g., the cases given by *Bird et al.* [1983]), with some rare two dimensional flow configurations where applying integral transforms to the governing equations places them in a separable form [e.g., *Craster*, 1995]. Viscoplastic fluid flow in a rectangular channel is not one of these simple cases. Some flawed models for this configuration have been previously proposed and cited in the literature [e.g., *Johnson*, 1970, section 15; *Taylor and Wilson*, 1997; *Tallarico and Dragoni*, 2000]. These models invoke physically incorrect assumptions and their results become increasingly inaccurate or physically impossible with increasing plasticity (Figure 3).

[1]Research School of Earth Sciences, Australian National University, Canberra, ACT, Australia.

0148-0227/12/2011JB008550

Figure 1. A lava flow on the east flank of Mt Etna at around 2800 m above sea level, looking east over the Valle del Bove towards the town of Giarre. More than a million people live within range of lava flows in the Catania region. Image taken on 5th October, 2008. Photo credit: Thomas Reichart.

[5] The development of numerical methods to investigate the dynamics of viscoplastic flow has been an active area of research for the last two decades (see *Dean et al.* [2007] for a review). Unfortunately, this literature is often focused on the development of solution algorithms and is thus unconcerned about providing results which can be easily applied to field or experimental studies from a volcanological perspective.

[6] To fill this gap and resolve previous mistakes in the literature we analyze viscoplastic flow in a rectangular channel and specifically discuss features which arise in volcanological studies in practice. In sections 2 and 3 we define and summarize the features of viscoplastic fluid rheology in general, and channel flows in particular, provide useful limiting cases which have analytical solutions, and clarify the numerical techniques used to obtain solutions for other cases. In sections 4 and 5 we present the results of our numerical calculations, and compare these to previously published models noted above. Section 6 outlines some algorithms for extending the results to a number of cases with different sets of measured parameters, and section 7 applies these methods to a typical lava flow on Mt Etna.

2. Viscoplastic Rheology

[7] A viscoplastic material behaves as a solid up to a critical magnitude of an applied shear stress, τ_y, called the yield strength. The material will deform upon exceeding the yield strength until the applied stress is either relaxed or removed [*Ancey*, 2007]. The simplest viscoplastic fluid model is the Bingham fluid, which consists of a combination of plastic and Newtonian rheologies. This fluid rheology was first introduced by *Bingham* [1916] for one dimensional flows and later extended to a multi-dimensional tensorial formulation by *Oldroyd* [1947]. This latter formulation relates the deviatoric stress tensor field, τ, to the strain rate tensor field, $\dot{\epsilon}$, within the fluid:

$$\tau = \begin{cases} \left(2\mu + \sqrt{2}\dfrac{\tau_y}{\|\dot{\epsilon}\|}\right)\dot{\epsilon} & \text{if } \|\tau\| \geq \tau_y \\ \dot{\epsilon} = 0 & \text{otherwise.} \end{cases} \quad (1)$$

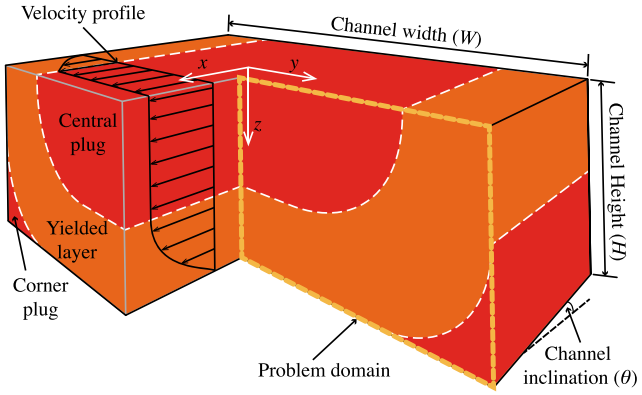

Figure 2. Schematic diagram showing the basic flow configuration, with a large central plug region and two corner regions separated by a yielded layer. Also shown is a schematic velocity profile along the flow surface and centreline. The orientation of the axes is shown, as well as the parameters describing the channel geometry. The problem domain is shown by the dotted box in the right hand half of the channel; due to the symmetric geometry of the channel, we need only consider one half of the cross-section when solving for the velocity field.

where μ is the plastic viscosity, τ_y the yield strength of the material and $\|\cdot\|$ denotes the Frobenius norm. More complicated rheologies (Herschel-Bulkley fluids for example) are also used as models for lava flows (see *Bird et al.* [1983] for a review).

[8] The Bingham rheology divides a viscoplastic flow into two sets of domains; one set is described by the first branch of the constitutive relationship given in equation (1), called 'yielded regions', in which the applied shear stress exceeds the yield strength and the fluid deforms. The second branch of equation (1) describes the 'plug regions'. In these regions the shear stress is low enough that the yield strength of the fluid prevents deformation. The 'yield surface' forms the

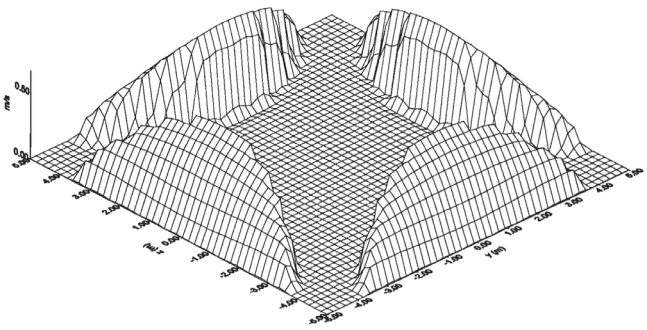

Figure 3. Figure 6c taken from *Tallarico and Dragoni* [2000], showing their solution for a flow in a square duct with a side length of 10 m. The relevant physical properties are $\tau_y = 10^4$ Pa, $g' = 1.95$ m s^{-2}, $\mu = 7 \times 10^3$ Pa s and $\rho = 2650$ kg m^{-3}. 'Seepage flows' occur beside the walls while the central plug remains welded to the corner plugs. This is a physically impossible solution, since if the central plug is not moving then there is nothing to provide the shear stress which is driving the flows at the walls (see also Figure 12).

boundary between plug and yielded regions (where $|\tau| = \tau_y$). The spatial derivatives of the strain rates are discontinuous across the yield surface; it is this aspect of the rheological model which makes direct solutions to viscoplastic flow problems difficult to obtain.

[9] For a given flow, the magnitude of the yield strength determines the location of the yield surfaces (and thus the size of the plug regions). As $\tau_y \to 0$ (so that the rheology approaches a Newtonian rheology with viscosity μ) the size of the plug regions and yield surfaces shrink to zero and the fluid yields everywhere. On the other hand, as the yield strength approaches a critical value, $\tau_y^\star$, the plug regions expand until the fluid is everywhere unyielded, and the flow ceases. $\tau_y^\star$ is dependent on the flow configuration; analytical expressions for it exist in some cases (including this one, see Appendix A).

[10] Given characteristic length and velocity scales L_0 and U_0 for some flow configuration, the relevant dimensionless parameter describing the rheology of the fluid in a dynamical sense is the Bingham number:

$$B = \frac{\tau_y L_0}{\mu U_0}, \tag{2}$$

which is simply the ratio of the yield strength to a characteristic viscous stress $\mu U_0/L_0$. A Newtonian fluid has a Bingham number $B = 0$, and there is also a critical value of the Bingham number, $B^\star$ corresponding to the critical yield strength $\tau_y^\star$. The flows under consideration therefore have Bingham numbers $0 \le B \le B^\star$.

3. Modeling Viscoplastic Channel Flows

[11] We now consider the main problem of this study: laminar flow of an incompressible Bingham fluid down a rectangular channel as shown schematically in Figure 2.

3.1. Parameters

[12] We specify the fluid density ρ, ambient fluid density ρ_a, inclination of the base of the flow θ (relative to horizontal) and width of the channel W. With these definitions the effective down-channel buoyancy force acting on the flow per unit mass is

$$g' = (1 - \rho_a/\rho) g \sin\theta.$$

where g is the acceleration due to gravity. We assume that the viscosity of the ambient fluid is much smaller than the viscosity of the Bingham fluid, so that the shear stress at the flow surface is negligible.

[13] In this study we focus on the following parameters in this flow configuration: the depth of the flow, H; the maximum velocity at the flow surface, U_m; the fluid viscosity and yield strength, defined above; the down-channel volumetric flow rate, Q; and the depth and width of the central plug, H_p and W_p. All of these parameters are interdependent: we can specify some of these and use them to constrain the unknown parameters.

[14] To define dimensionless parameters, we choose the flow depth H as a characteristic length scale. Since buoyancy is the only force driving the flow, dimensional reasoning shows that the relevant velocity scale is $g'H^2/\nu$, where $\nu = \mu/\rho$ is the dynamic viscosity of the yielded fluid. The dimensionless parameters obtained from this scaling are the Bingham number (from equation (2)):

$$B = \frac{\tau_y}{\rho g' H} \tag{3}$$

and the aspect ratio of the flow cross-section, given by:

$$\beta = \frac{W}{H}. \tag{4}$$

[15] We also obtain a Reynolds number,

$$Re = \frac{g' H^3}{\nu^2},$$

which must be small ($Re < 10^2$) for the flow to be laminar, but otherwise plays no further role in describing the dynamics.

[16] We define the central plug depth and width fractions as

$$h_p = \frac{H_p}{H} \text{ and } w_p = \frac{W_p}{W}$$

respectively. The scaling given above also gives a dimensionless maximum velocity of

$$u_m = \frac{\nu U_m}{g' H^2}$$

and a flow rate per unit width of

$$q = \frac{\nu Q}{g' W H^3}.$$

[17] In this setting the flow rate per unit width is useful as it approaches a constant in the limit of an infinitely wide flow (i.e. as $\beta \to \infty$), whereas the total flow rate becomes infinite.

3.2. Governing Equations

[18] We choose the axes so that flow travels in the x direction, with the y direction across the channel and the z direction perpendicular to the channel floor (see Figure 2). Incompressibility and the assumption of laminar flow ensures that the velocity field is invariant along the x axis, and the only non-zero component of the velocity field is the x-component $u(y, z)$. Then the problem domain reduces to a cross-sectional slice of the channel, and the remaining component of the momentum equation is

$$\left.\begin{aligned} \nabla^2 u - B\nabla \cdot \left(\frac{\nabla u}{|\nabla u|}\right) = -1 \quad & \text{where } \tau^2 \ge B^2 \\ \nabla u = 0 \quad & \text{where } \tau^2 < B^2 \end{aligned}\right\} \tag{5}$$

where τ is the dimensionless shear stress field.

[19] The velocity field satisfies no-slip conditions on the channel walls and a no-shear condition at the flow surface. Since the problem domain and the boundary conditions are symmetric about the center plane $y = 0$, we need only solve for the velocity field in half the channel ($0 \le y \le \beta/2$ and $0 \le z \le 1$) with a no-shear condition on the channel center line.

Putting this all together we have the following boundary conditions on u:

$$\left.\begin{array}{c} u = 0 \text{ for } y = \beta/2 \text{ or } z = 1 \\ \partial u/\partial y = 0 \text{ for } y = 0 \\ \partial u/\partial z = 0 \text{ for } z = 0 \end{array}\right\} \quad (6)$$

[20] We note that this problem is also equivalent to the case of a no-slip condition at the flow surface (e.g. in a full lava tube), where by a similar symmetry argument the problem domain specified here corresponds to quarter of the actual flow domain.

3.3. Solution Methods

[21] Any method used to solve equations (5) and (6) needs to find some way of dealing with the singularity in strain rate gradients at the yield surface as part of the solution. We mention in passing one popular solution, which has been to employ a 'regularization approach' [*Papanstasiou*, 1987; *Taylor and Wilson*, 1997], which replaces the two branches of equation (5) with the following nonlinear elliptic problem:

$$\nabla^2 u - B\nabla \cdot \left(\frac{\nabla u}{|\nabla|u + \varepsilon}\right) = -1 \quad (7)$$

where ε is a small positive parameter, known as the regularization parameter. The effect of this substitution is to 'smooth out' the singular behavior of the rheology so that the fluid has one smoothly varying effective viscosity. Specifically ε represents a transition strain rate between a high effective viscosity rheology for $\dot{\gamma} < \varepsilon$ (where the dimensionless apparent viscosity $\eta = \dot{\gamma}/\tau$ is approximately $O(B/\varepsilon)$) and a low-viscosity rheology for $\dot{\gamma} > \varepsilon$ (where $\eta \sim O(1)$).

[22] Unfortunately solutions to the regularized problem in equation (7) do not have true plug regions as all of the fluid can yield at least slightly, and thus there are no yield surfaces. Making the regularization parameter smaller improves the distinction between plug and yielded regions, however the increasing nonlinearity means calculation time becomes prohibitive, especially in the physically interesting cases where the Bingham number approaches its critical value.

[23] We have instead elected to use an algorithm based on energy minimization. We sketch an overview of the algorithm used here and refer interested readers to the detailed development given by *Glowinski and Le Tallec* [1989]. Using thermodynamic reasoning, *Il'iushin* [1940] showed that the flow of a Bingham fluid minimized an energy functional, and obtained the form of the functional which takes into account the two components of energy dissipation in the yielded fluid domains (corresponding to the yield strength and the yielded fluid viscosity). *Mosolov and Mjasnikov* [1965] then used this minimization principle to analyze the solutions to equations (5) and (6) without knowing the location of the yield surface *a priori*. Their analysis allows the development of an algorithm in which the nonlinearity in the governing equations is decoupled by treating the velocity field u and the dimensionless strain rate vector $\dot{\gamma}$ (obtained as the gradient of the velocity field) as separate variables, and a Lagrange multiplier λ is employed to enforce the condition $\dot{\gamma} = \nabla u$. We use an Uzawa-type algorithm to solve the resulting saddle problem. The result is the algorithm given by *Glowinski and Le Tallec* [1989] (their Algorithm 4.20–4.23 on p. 84).

[24] The algorithm proceeds as follows: find an initial estimate of the velocity field by solving the following Poisson problem for u_0:

$$(1 + \alpha)\nabla^2 u_0 = -1, \quad (8)$$

where u_0 satisfies the boundary conditions given in equation (6). Then take $\lambda_1 = 0$, and for $n \geq 1$, given u_{n-1} and λ_n:

[25] 1. Calculate $\dot{\gamma}_n$ using:

$$\dot{\gamma}_n = \begin{cases} \left(1 - \dfrac{B}{|s_n|}\right)\dfrac{s_n}{\alpha} & \text{if } |s_n| \geq B, \\ 0 & \text{otherwise.} \end{cases} \quad (9)$$

where

$$s_n = \alpha\nabla u_{n-1} + \lambda_n.$$

[26] 2. Find u_n such that:

$$(1 + \alpha)\nabla^2 u_n = \nabla \cdot (\alpha\dot{\gamma}_n - \lambda_n) - 1, \quad (10)$$

where u_n satisfies the boundary conditions given in equation (6).

[27] 3. Update the multiplier λ:

$$\lambda_{n+1} = \lambda_n + \alpha(\nabla u_n - \dot{\gamma}_n). \quad (11)$$

[28] 4. Check for convergence; the algorithm has converged if, for some tolerance δ:

$$\frac{\|\nabla u_n - \dot{\gamma}_n\|}{\|\nabla u_n\|} \leq \delta \quad (12)$$

[29] 5. If the convergence test fails, replace n with $n + 1$ and return to the first step.

[30] In this algorithm α is a positive parameter. This augmented formulation improves the conditioning of the Lagrangian minimization problems. Tuning the value of α can give better algorithm convergence, although the optimum value of α is dependent on the Bingham number and aspect ratio. If α is too low, the algorithm will converge rather slowly, while too high a value of α results in instability, especially in the plug regions of the flow.

[31] A number of studies use the algorithm (8–12) in slightly different forms [e.g., *Saramito and Roquet*, 2001; *Dean et al.*, 2007]. These studies usually solve the linear problem in equation (10) using finite element methods at each iteration. Given the rectangular domain under consideration, we employ finite differences using a full multigrid algorithm. This method has the advantage of being fast, and easier to develop than a finite-element code. We base our multigrid solver (written in C++) for equation (10) on the version given by *Press et al.* [1992, section 19].

[32] We calculated flow solutions for 1666 flow configurations: these had 49 aspect ratios between $1/5 \leq \beta \leq 25$, with 34 values of the Bingham number per aspect ratio. We only performed actual calculations for flows with $\beta \geq 2$, since cases with $\beta < 2$ can be obtained from these results via the symmetry of the flow configuration (i.e. by swapping H and W and rescaling other values).

[33] The computation for $\beta = 2$ was calculated on a 384×384 grid with eight coarser grids based on this fine

grid; the coarsest grid in the solver had a minimum resolution of 4×4 grid points. For higher aspect ratios the x-resolution was increased to keep the resolutions in the x and z directions the same. The number of iterations required for convergence of the algorithm (8–12) ranged between 1 for Newtonian flows (with $B = 0$) to around 1000 iterations for Bingham flows with $B = 0.95B^\star$, but with a median of order 100 iterations for most configurations. Computations were run in parallel on an 8-core Mac Pro.

3.4. Useful Limiting Cases

[34] While there are no analytical solutions for the general case of a rectangular cross-section for arbitrary aspect ratio and Bingham number, solutions do exist for infinitely-wide flows with $0 \le B \le 1$ and the Newtonian case ($B = 0$) for all aspect ratios. The critical Bingham number for a rectangular flow cross-section is also given by analytic expressions. These can provide useful checks on the numerical calculations, and we summarize them here.

3.4.1. Two Dimensional Flows

[35] A film flow is a flow with infinite width and constant depth. Channel flows approach this limit as $\beta \to \infty$. The down-channel velocity varies in z only, and the solution is:

$$u(z) = \begin{cases} \dfrac{2(1-B)z - z^2}{2} & \text{for } 0 \le z < 1 - B \\ \dfrac{(1-B)^2}{2} & \text{for } 1 - B \le z \le 1. \end{cases}$$

[36] Then the maximum velocity is

$$u_m = \frac{(1-B)^2}{2}, \tag{13}$$

and by integrating u through the flow depth we obtain the flow rate per unit width:

$$q = \frac{2 - 3B + B^3}{6}. \tag{14}$$

[37] In this case, the Bingham number is simply the depth of the plug region, i.e. $B = H_p/H$. The Bingham number must therefore be less than the critical value $B^\star = 1$ for there to be any flow.

3.4.2. Newtonian Channel Flows

[38] The analytic solution for a Newtonian channel flow provides another useful bound on the limit $B \to 0$. In this case the governing equation reduces to the Poisson equation, which has the (dimensionless) analytical solution [*White*, 1990]:

$$u = \frac{16}{\pi^3 \beta^2} \sum_{k=1}^{\infty} \frac{(-1)^{k-1}}{(2k-1)^3} \left[1 - \frac{\cosh(\zeta_k)}{\cosh(\zeta_k \beta/2)}\right] \cos(\zeta_k (1 - z)), \tag{15}$$

where $\zeta_k = (2k-1)\pi/2$. The maximum velocity for this flow is along the center line $y = 0$ and $z = 1$, giving:

$$u_m = \frac{1}{2} - \frac{16}{\pi^3} \sum_{k=1}^{\infty} \frac{(-1)^{k-1}}{(2k-1)^3} \operatorname{sech}\left(\frac{\zeta_k \beta}{2}\right). \tag{16}$$

[39] By integrating across the channel cross section and dividing by the aspect ratio we obtain the dimensionless down-channel flow rate per unit width:

$$q = \frac{1}{3} - \frac{128}{\pi^5 \beta} \sum_{k=1}^{\infty} \frac{1}{(2k-1)^5} \tanh\left(\frac{\zeta_k \beta}{2}\right). \tag{17}$$

3.4.3. Critical Bingham Numbers

[40] A final case of interest is the set of conditions under which flow ceases. This occurs at a critical value of the yield strength $\tau_y^\star$; for flow in a rectangular channel it is

$$\tau_y^\star = \rho g' \frac{W + 2H - \sqrt{4H^2 + W^2 - (2\pi - 4)HW}}{4 - \pi}. \tag{18}$$

Appendix A gives the derivation of this expression, which follows the analysis of *Mosolov and Mjasnikov* [1965]. This yield strength corresponds to a critical Bingham number

$$B^\star = \frac{2 + \beta - \sqrt{4 + \beta^2 + (2\pi - 4)\beta}}{4 - \pi}. \tag{19}$$

From this we see that $B^\star$ ranges from 1 for a film flow ($\beta \to \infty$) to $B^\star = 0$ for the case of a slot flow (as $\beta \to 0$).

[41] An alternative is to consider the case of zero flow rate for a given value of B; the critical central plug shape $\omega^\star$ (found in Appendix A) which corresponds to $B^\star$ represents a lower bound on the geometry obtainable by a viscoplastic flow in the same way as viscoplastic film flows have a minimum thickness. In this case, we obtain a minimum aspect ratio $\beta^\star$ expressed in terms of a given Bingham number B:

$$\beta^\star = \frac{(\pi - 4)B^2 + 4B}{2 - 2B} \tag{20}$$

Note these critical yield strengths values are only attainable in fixed aspect ratio flows. In the case of a non-zero flow rate and variable flow geometry, the flow will simply inflate to match the flow rate condition, such that $B < B^\star$.

4. Results

[42] We first examine the behavior of the flow for fixed aspect ratio β and varying Bingham number B. Figure 4 shows plots of the down-stream velocity and strain rate tensor magnitude fields for three flows with $\beta = 2$ and three different values of B. In this case the critical Bingham number is

$$B^\star = \frac{2}{2 + \sqrt{\pi}} \approx 0.530; \tag{21}$$

all the plotted flows have $0 \le B < B^\star$.

[43] For the two Bingham cases, dotted black lines delineate the yield surfaces, and the shading denotes the plug regions. In the Newtonian case the entire fluid yields, however the two plug regions grow with the development of a yield strength. One plug region forms in the corner of the channel, fixed to the channel walls with a concave circular arc forming the yield surface, while one forms around the channel center, and moves at the maximum velocity in the

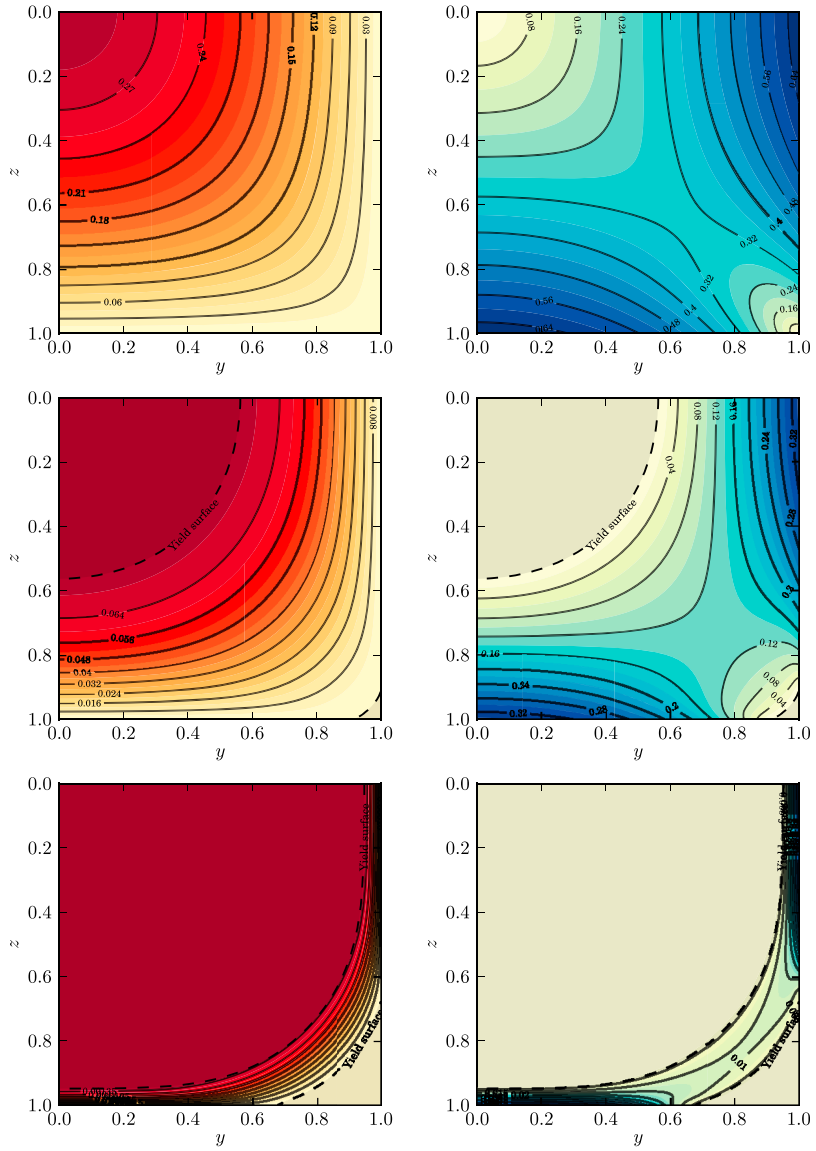

Figure 4. Contour plots of the (left) the velocity and (right) strain rate magnitude for a channel with aspect ratio of $\beta = 2$, and Bingham numbers of $B = 0$, 0.274 and 0.496. The definitions of Bingham number and aspect ratio are given in equations (3) and (4). The critical Bingham number for this aspect ratio is approximately 0.530 (see (21)). The yield surface is shown as a dashed line and the plug regions are shaded. Only half of the channel is shown as these distributions are symmetrical about the center line of the channel.

channel. At low values of B the central plug is almost circular, but as B increases the sides of the center plug flatten as they approach the walls, although the corners remain circular.

[44] A layer of yielded fluid separates the two plug regions. The strain rate magnitudes in Figure 4 show that the strain rate drops to zero at the plug boundaries. The strain rate magnitude reaches a maximum at the center of the channel floor and the top of the channel walls, with a saddle point in the center of the yielded layer between the plug regions. This layer is widest on the diagonal of the domain between the two plug regions, and narrows as it approaches the flow surface or center line.

[45] As the Bingham number increases (moving from top to bottom), the size of the central and corner plug regions increases until they meet at the critical Bingham number and flow ceases (not shown). The central plug grows at a faster rate than the corner plug. The width of the yielded layer between the plug regions narrows and the velocity of the central plug decreases, such that the yielded layer thickness goes to zero everywhere upon reaching the critical Bingham number.

[46] Figure 5 shows the behavior of the channel flow for a fixed Bingham number of 0.5 and variable aspect ratio. Given B, equation (20) gives the minimum aspect ratio of

$$\beta^{\star} = \frac{4+\pi}{4} \approx 1.785. \tag{22}$$

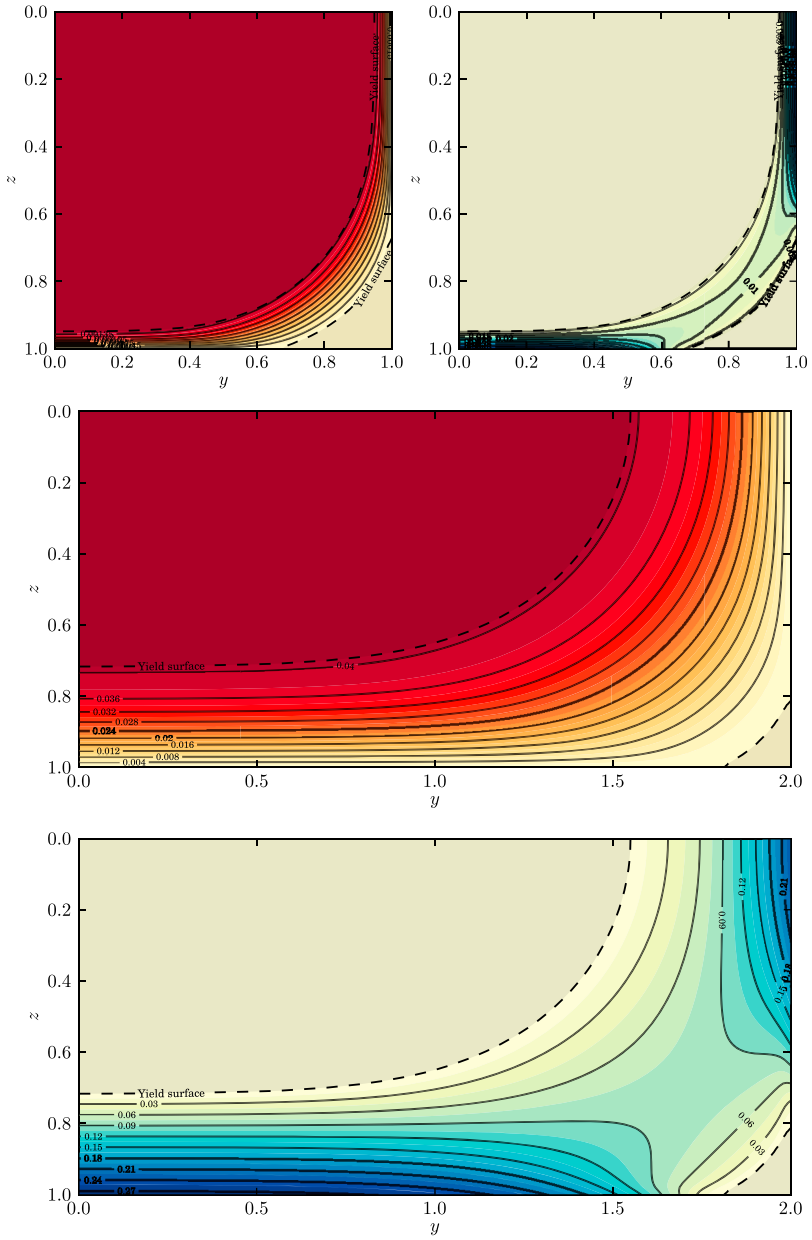

Figure 5. Contour plots of the velocity and strain rate magnitude for a channel flow with a Bingham number of $B = 0.5$, and aspect ratios of $\beta = 2$ and 4. The critical aspect ratio for this Bingham number is approximately 1.785 (see (22)). The yield surface is shown as a dashed line and the plug regions are shaded.

[47] The size of the corner plugs remain similar in all of these cases, and the first-order effect of the varying aspect ratio is thus to alter the aspect ratio of the central plug. The central plug thickness decreases as the aspect ratio increases, due to the decreasing drag exerted by the walls as they move further apart. In contrast, the plug width (scaled to the channel width) increases throughout the range of aspect ratios, although the width of the yielded layer at the surface of the flow increases with increasing aspect ratio. Similarly the thickness of the yielded layer on the channel center line approaches the limiting two-dimensional value of 0.5 as $\beta \to \infty$.

[48] Figure 6 shows the convergence of flow parameters taken from the calculated solutions towards those of the analytic two-dimensional film flow limit as $\beta \to \infty$. Solid black lines denote the two-dimensional solutions (given in section 3.4.1) in all plots, while colors show the value of the aspect ratio. The top two plots show the calculated flow per unit width and the maximum velocity converging towards that of the two-dimensional limit. The maximum velocity converges faster than the flow rate; the velocity is within 10% of the two-dimensional value at $\beta = 5$, while the flow rate is within 10% only by $\beta \approx 15$. The bottom plot shows that the plug depth converges only slightly slower than the

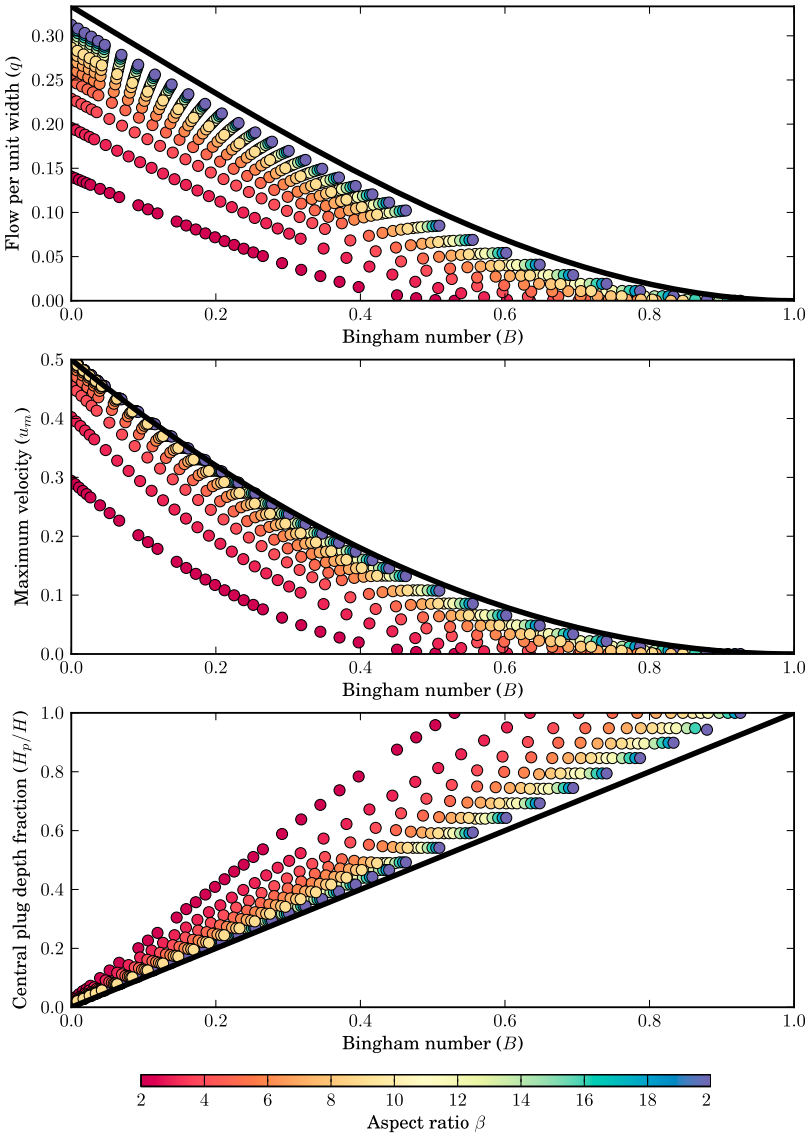

Figure 6. Convergence of calculated values for (top) flow rate, (middle) maximum velocity and (bottom) central plug depth towards the two dimensional film flow limit (see section 3.4.1). Each dot represents a calculation, colored by aspect ratio β (colors are the same for all plots). In all plots the solid black line denotes the limiting two dimensional flow value; the limit in the case of the central plug width fraction is $w_p/w = 1$ for all Bingham numbers.

flow rate. We suggest that the two-dimensional flow solution makes a good approximation for the flow rate, maximum velocity and central plug depth above $\beta \approx 15$.

[49] Similarly, Figure 7 shows the convergence of the flow rate per unit width, the maximum surface velocity and the ratio of central plug width to channel width towards the Newtonian analytic solution given in section 3.4.2 as $B \to 0$. The solid black line represents the Newtonian analytic solution and the colors show the value of B for each calculation. The flow rate and maximum velocity plots converge smoothly towards the Newtonian analytical limit. In contrast the plug width fraction does not approach the Newtonian limit ($W_p/W = 0$ for all β) in the same manner; there is a rapid variation in plug width between the Newtonian and weakly Bingham flows at high aspect ratio. This is because the majority of the surface shear strain occurs over a distance of order H from the walls; thus it only takes a small yield strength to jump from no surface plug to a plug width of about $W - 2H$, particularly at large aspect ratios.

[50] Figures 8 and 9 show the flow rate per unit width and maximum velocity as functions of the aspect ratio and Bingham number, contoured from the values obtained from 1504 flow configurations. Figures 10 and 11 show similar plots for $h_p = H_p/H$ and $w_p = W_p/W$, i.e. the plug width and height scaled to the channel width and height. The contours in all four plots have been found by triangulating the flow configuration data and using a linear barycentric interpolant on each triangle (i.e. a piecewise-linear two-dimensional interpolation).

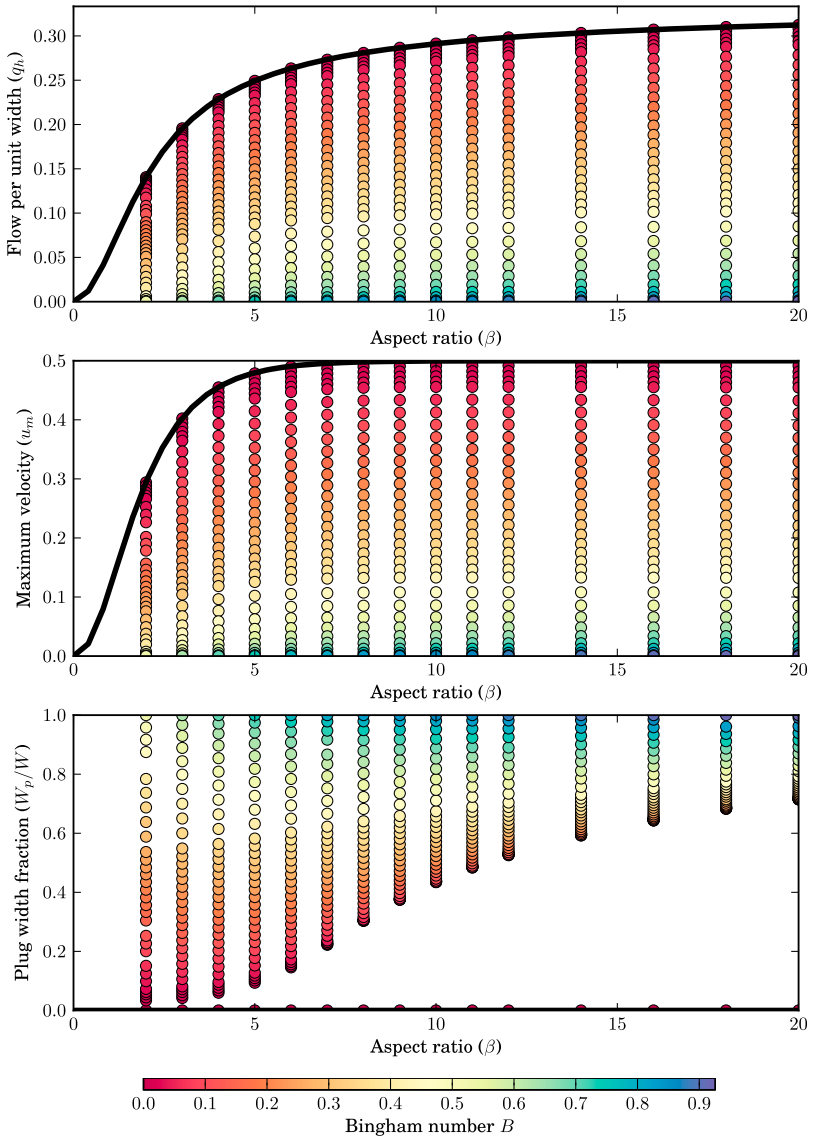

Figure 7. Convergence of calculated values for (top) flow rate, (middle) maximum velocity and (bottom) the ratio of central plug width to channel width towards the limit of a Newtonian viscous rheology. Each dot represents a calculation, colored by Bingham number B (the colors are the same for all plots). In all plots the solid black line denotes the expected value when $B = 0$ (expressions are given in section 3.4.2).

[51] In all of these plots the critical Bingham number $B^\star$ given by equation (19) forms the upper boundary of the data — supercritical configurations with Bingham numbers beyond this limit will not flow. As expected, this line also forms the contour of zero flow rate and zero maximum velocity for all the plots, as well as plug height and width fractions of 1. The two dimensional limit would fall at the far right hand side of the plots, and the Newtonian limit forms the bottom, along $B = 0$.

5. Comparisons With Previous Studies

[52] *Johnson* [1970] presented a study aimed at explaining the dynamics of slurry flows and erosion patterns in glacial valleys. He defined a model of viscoplasticity using an internal angle of friction to account for the yielding behavior of the fluid (similar to analysis of finite-displacement problems with plastic materials). He then derived a set of governing equations by inserting this rheological model into the momentum balance for a fully-developed flow.

[53] There are two flaws in Johnson's analysis. The first is in his formulation of the three-dimensional rheology, whose energy balance (his equation 15.38, pp. 553) does not take into account the energy dissipation produced by the yield strength of the fluid in yielded regions. The second is the decomposition of the stress field into a Fourier series (in his equation 15.44, on p. 554). To apply a Fourier decomposition the stress fields must be superposable so that all modes of the decomposition contribute equally to the velocity field. This superposition is only valid for linear (i.e. Newtonian) fluid rheologies. In contrast, non-Newtonian fluids have

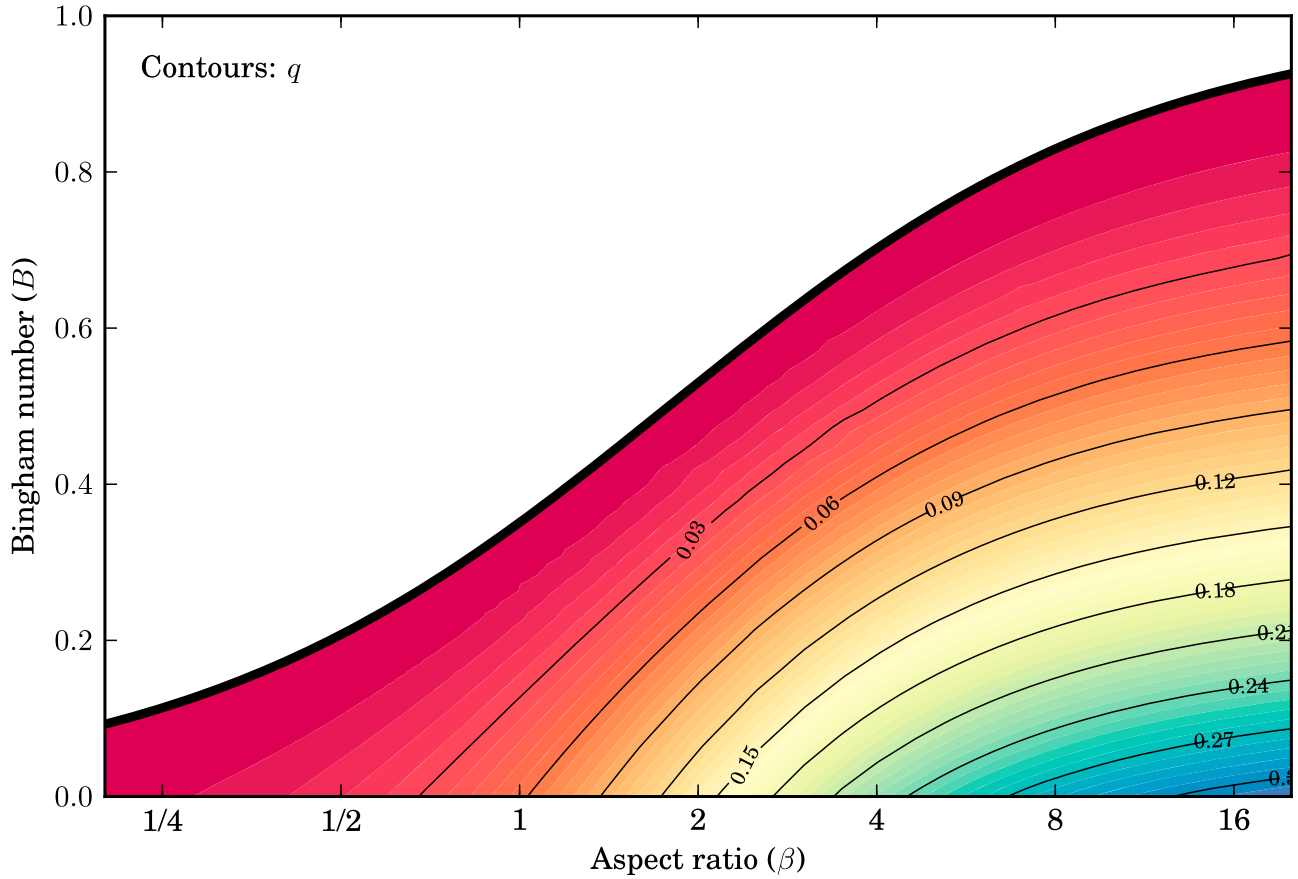

Figure 8. Calculated dimensionless flow rate per unit width q plotted as a function of aspect ratio β and Bingham number, B. The heavy black line denotes the critical Bingham number $B^{\star}(\beta)$, given in equation (19).

stress fields which are not decomposable into Fourier modes in general. The effect of Johnson's analysis is to recover the stress field for a purely Newtonian flow, ignoring the contribution of the energy dissipation by the yield strength to the energy balance in yielded portions of the flow.

[54] Similarly, *Tallarico and Dragoni* [2000] present an semi-analytical model for the duct flow of a viscoplastic fluid with a Bingham rheology, based on a similar analysis to *Johnson* [1970]. Their model involves a calculation of the vorticity of the down-channel velocity field, which is then inverted for the velocity profile across the channel cross-section. The authors derive governing equations for the vorticity vector field by taking the curl of the Navier-Stokes equations, which they assert describes the motion of a Bingham fluid.

[55] The flaw in Tallarico and Dragoni's analysis is the use of the Navier-Stokes equation, which assume a Newtonian rheology in their derivation. They do not describe the behavior of a viscoplastic fluid at all. To see this, note that we can represent both Newtonian and many non-Newtonian rheologies using an effective viscosity η: for Newtonian flows $\eta = \mu$ is constant, for non-Newtonian flows η will be strain- or stress-dependent and will vary with position in the flow. The governing equations for the vorticity vector, ξ, are then found by taking the curl of the (low Reynolds number) equation of motion with the relevant constitutive equation for an effective viscosity η, giving

$$\nabla \cdot (\eta \nabla \xi) = 0.$$

In the Newtonian case expansion of this equation gives Laplace's equation

$$\nabla^2 \xi = 0.$$

In the non-Newtonian case the expansion of this equation is more complex:

$$\eta \nabla^2 \xi + \nabla \eta \cdot \nabla \xi = 0.$$

The second part of this expanded term is small for weakly non-Newtonian fluids (for which the spatial gradients in effective viscosity are small), but becomes more important as the rheological nonlinearity increases. Tallarico and Dragoni's analysis misses this important nonlinear term.

[56] These flawed assumptions in the models of Tallarico and Dragoni and Johnson have significant consequences for the results which they obtain from their models. Figure 12 compares the results obtained by the methods of *Tallarico and Dragoni* [2000] (which give the same answers as those of Johnson) with those of the current study. There are several important differences:

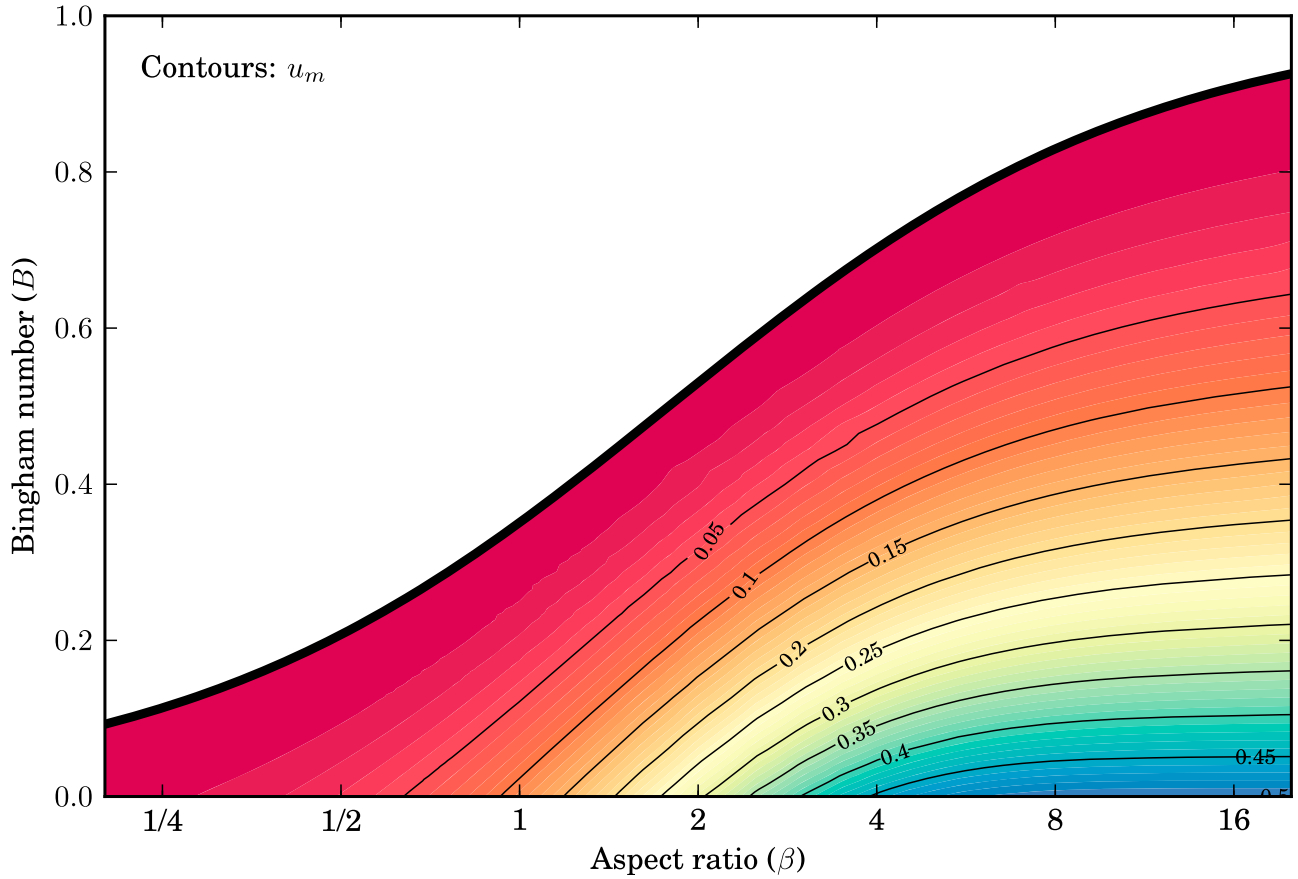

Figure 9. Calculated maximum surface velocity u_m plotted as a function of aspect ratio β and Bingham number, B.

[57] 1. In the models of Johnson and Tallarico and Dragoni a change in yield strength does not produce any change in the stress field calculated for the yielded portions of the flow. As can be seen from our solutions in Figure 12 (right), a change in fluid rheology should change the stress field throughout the entire flow, not just in the plug regions.

[58] 2. The shape of the corner plugs is incorrect. Both authors have corner plugs with a convex shape which protrudes into the main flow, whereas mathematical analysis of this problem shows that these zones should be concave [*Mosolov and Mjasnikov*, 1967] as obtained by the current calculations. It is difficult to see why these zones should protrude at all into the flow since the tip of the plug would be subject to high stresses from the remainder of the fluid, presumably exceeding the yield strength. The shape of the central plug also has this unintuitive feature, with a protrusion which grows towards the corner plugs as the Bingham number increases. As our study shows, the central plug should remain circular until the walls start to have an appreciable effect.

[59] 3. Both authors obtain incorrect values for the critical Bingham number where the central plug meets the corner plug, again a result of the incorrect shape of the modeled plugs. In the example given in Figure 12 the critical Bingham number lies between the $B = 0.3$ and $B = 0.35$ examples, which is markedly different to the expected analytical value of about 0.530 (given in equation (21)).

[60] 4. The models of both authors produce an unphysical solution at supercritical Bingham numbers where the fluid 'seeps' around the central plug which sticks to the corner plugs (with the velocity field from *Tallarico and Dragoni* [2000] shown in Figure 3, and the strain rate magnitude in Figure 12 (bottom left)). It is difficult to see what is driving these seepage flows if the central plug is not moving (a fact acknowledged by Johnson).

[61] 5. Finally, the nature of Bingham constitutive equation implies that plug regions should form around all local maxima or minima in the velocity field, since the shear stress must necessarily fall beneath the yield strength in the regions where $|\nabla u| \to 0$. The supercritical solutions from both models do not satisfy this requirement as the seepage flows near the walls do not have plugs in their centers. As noted by both sets of authors, their models also fail to capture the transition from subcritical Bingham number flow to their supercritical seepage flow. As our results show, with a correct model the yielded layer disappears everywhere at the critical Bingham number, so that any flow at supercritical Bingham numbers is not possible with a purely Bingham rheology.

6. Applications

[62] As noted when describing channel flows in section 3.1, the choice of independent parameters used to describe channel

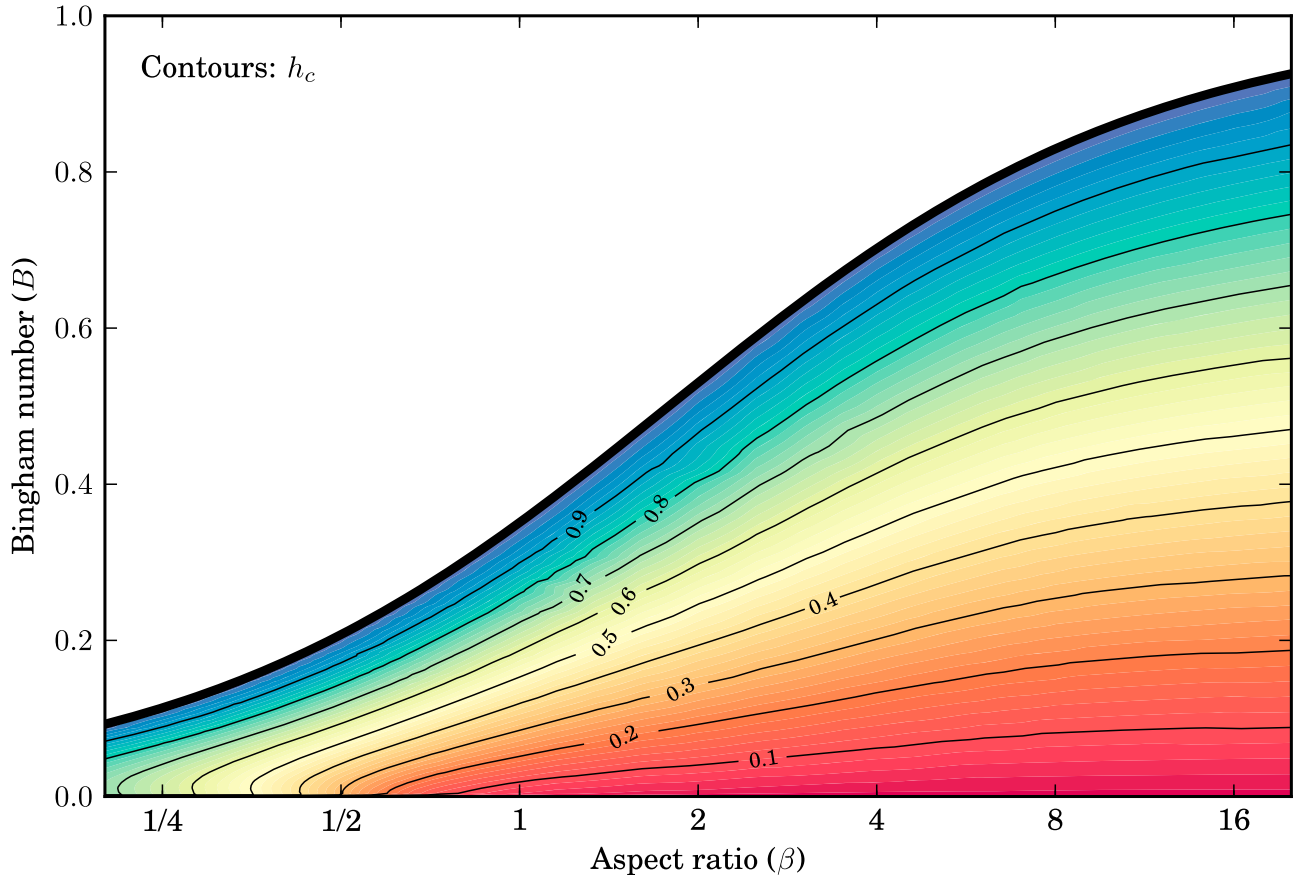

Figure 10. Calculated plug depth fraction, H_p/H plotted as a function of aspect ratio β and Bingham number, B. Note that when $\beta \ll 2$ and B is small, the plug depth drops rapidly to zero.

flows is application driven. In practice, variables such as the flow depth, fluid viscosity or yield strength are not always known beforehand, so that determining β and B is not straightforward. In this section we outline algorithms which can be used to apply the results of section 4 to these situations.

6.1. Flows With Dynamics Controlled by Flow Rate

[63] In the first application we solve the following problem:

$$\text{Given } Q, \nu \text{ and } \tau_y, \text{ determine } H, U_m \text{ and } W_p.$$

This application arises in experimental situations, where the flow rate and fluid properties control the dynamics of analogue flows. It is also applicable in field situations when trying to determine the downstream flow configurations for a given flow when the flow rate is prescribed by measurements upstream.

[64] Since β and B are not dependent on U_m, we can solve for H only and then separately calculate the maximum velocity and central plug width. We solve this problem with a secant root finding method against the cost function

$$f(H) = 1 - \frac{g' W H^3}{\nu Q} q(\beta, B), \tag{23}$$

where q is the dimensionless flow rate per unit width calculated from the interpolations given in Figure 8 with β and B evaluated for our current approximation to the flow depth H.

[65] The algorithm initialization requires two initial approximations to the flow height, H_0 and H_1. For H_0 we use the minimum flow depth $H^\star$ for the given yield strength and flow width by rearranging equation (20) to give:

$$H^\star = \frac{2W - (\pi - 4)\tau_y/\rho g'}{2W \rho g'} / \tau_y - 4. \tag{24}$$

For H_1 we take the height of a Newtonian two dimensional flow with the same flow rate per unit width, with a plug of depth $H^\star$ on top. Thus:

$$H_0 = H^\star \text{ and } H_1 = H^\star + \left(\frac{3\nu Q}{g' W}\right)^{1/3}. \tag{25}$$

We also need an initial value for the cost function: evaluating equation (23) at H_0 gives $f(H_0) = 1$, since $q = 0$ when $H = H^\star$.

[66] Then for $n > 1$, with H_{n-1} and H_n known, we iterate the following three step procedure:

[67] 1. Evaluate the cost function $f(H_n)$ using equation (23) and check for convergence; the algorithm has converged if

$$|f(H_n) - f(H_{n-1})| \le \delta$$

for some tolerance δ. If the algorithm has converged, use H_n to calculate β and B and use these to find U_m and W_p.

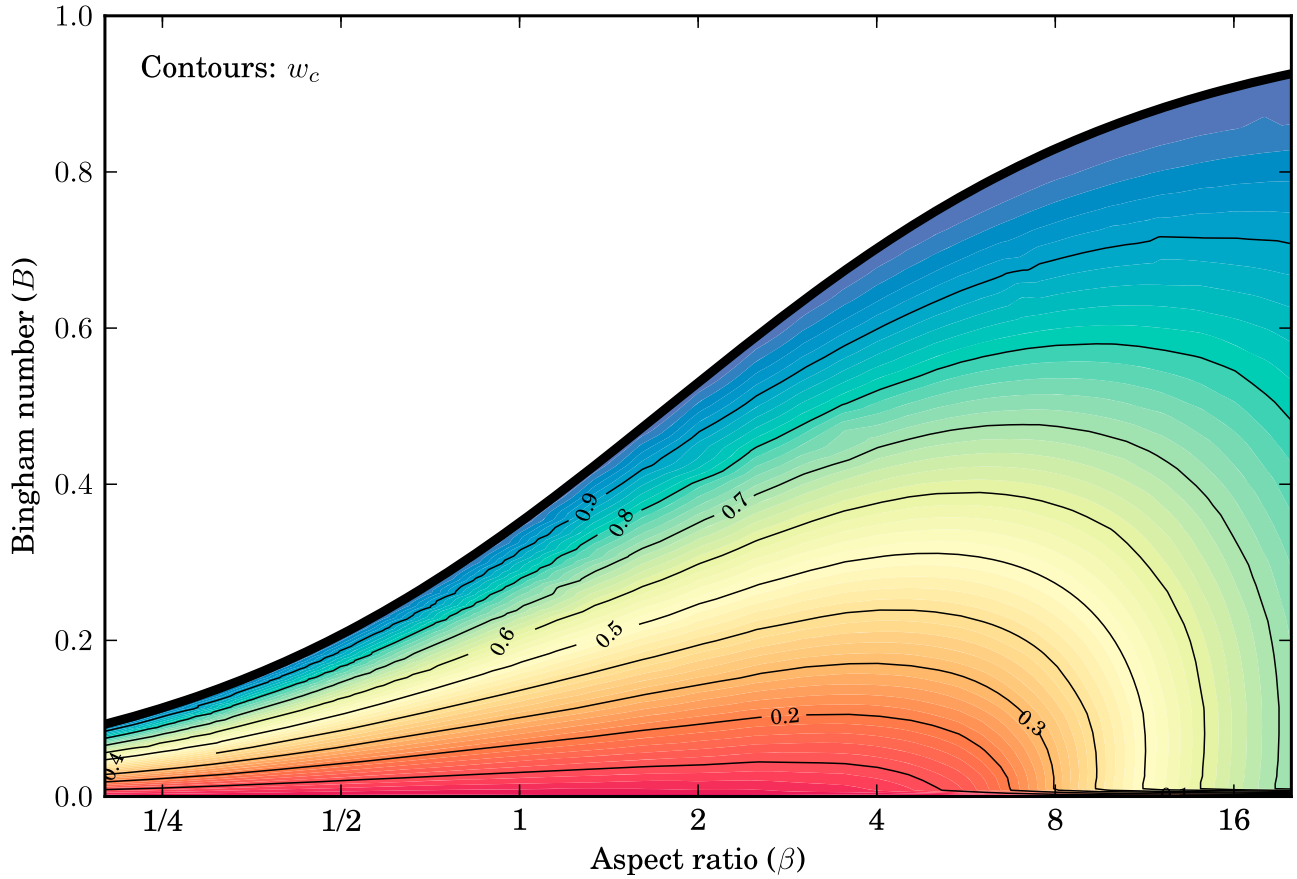

Figure 11. Plug width fraction, W_p/W, plotted as a function of aspect ratio β and Bingham number, B.

[68] 2. If the convergence test fails, update the approximation to H:

$$H_{n+1} = H_n - \frac{H_n - H_{n-1}}{f(H_n) - f(H_{n-1})} f(H_n).$$

[69] 3. Replace n with $n + 1$ and return to step 1.

6.2. Calculating Flow Rate and Height From Maximum Velocity

[70] If we know the maximum velocity but not the flow rate or height we have the following problem:

$$\text{Given } U_m, \nu \text{ and } \tau_y, \text{ determine } H, Q \text{ and } W_p.$$

Here the algorithm in section 6.1 can be used with the following cost function based on the maximum surface velocity (rather than equation (23) which is based on flow rate)

$$f(H) = 1 - \frac{g' H^2}{\nu U_m} u_m(\beta, B)$$

where β and B are evaluated using H and with

$$H_0 = H^\star \text{ and } H_1 = H^\star + \left(\frac{2\nu U_m}{g'}\right)^{1/2}$$

in the initialization (rather than equation (25)). Again, $f(H_0) = 1$ since $u_m = 0$ when $H = H^\star$.

6.3. Estimation Rheology From Flow Depth and Maximum Velocity

[71] If we have estimates for the channel depth, maximum velocity and surface plug width, and we require estimates for the flow rate and fluid rheology we have the following problem:

$$\text{Given } H, U_m \text{ and } W_p, \text{ determine } Q, \nu \text{ and } \tau_y.$$

This application could be useful in cases where field and geodetic observations of active flow fields provide measurements of the flow depth and surface velocities, giving a maximum velocity and an estimate of plug width [e.g., *Calvari et al.*, 2002; *Favalli et al.*, 2010].

[72] The difficulty in solving this problem is that we must solve for the viscosity and yield strength simultaneously. We can however constrain the rheological parameters separately from the flow rate, since β and B are not directly dependent on Q. For convenience, we form a vector of unknown variables:

$$\mathbf{x} = \begin{bmatrix} \nu \\ \tau_y \end{bmatrix}.$$

Then we require two constraints, in this case the measured values of W_p and U_m, and a vector cost function:

$$\mathbf{f}(\mathbf{x}) = \begin{bmatrix} 1 - \dfrac{g' H^2}{\nu U_m} u_m(\beta, B) \\ 1 - \dfrac{W}{W - W_p}\left(1 - w_p(\beta, B)\right) \end{bmatrix} \tag{26}$$

where β and B are evaluated using the current values in $\mathbf{x}$.

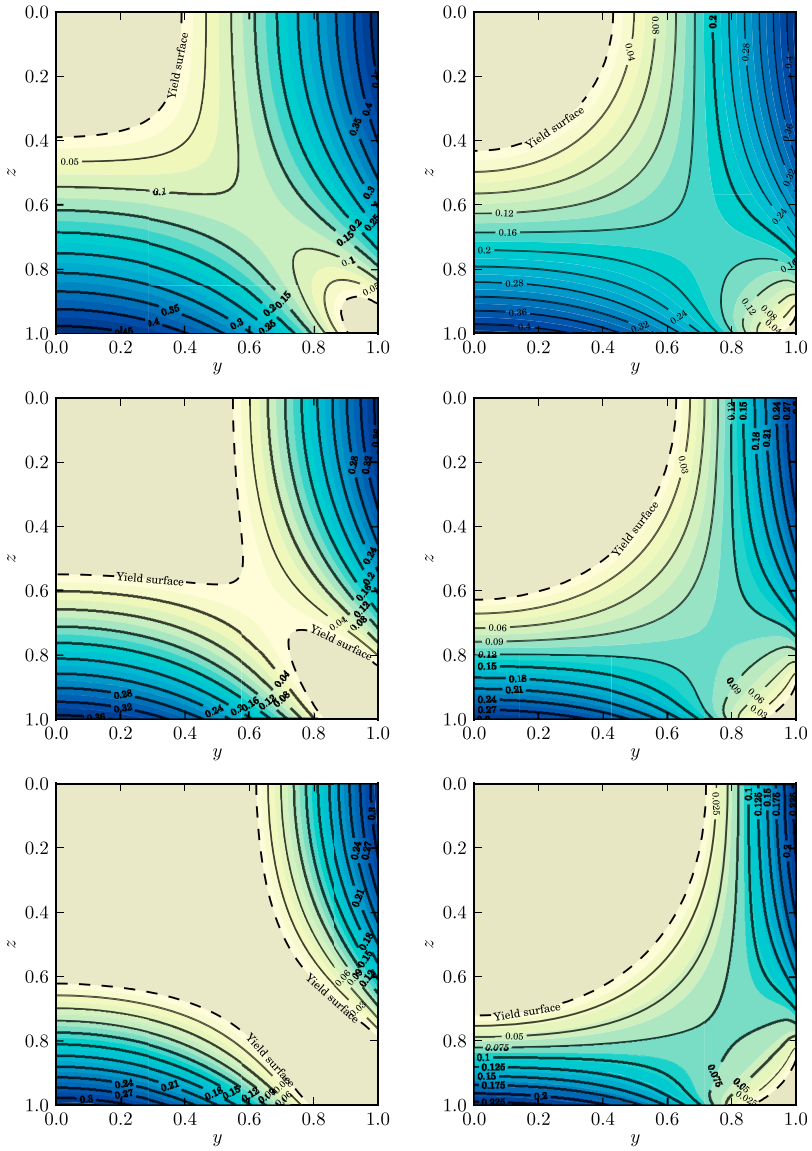

Figure 12. Contour plots of the strain rate magnitude field calculated from (left) the model of *Tallarico and Dragoni* [2000] and (right) the solver from this study. These flows have $\beta = 2$, and $B = 0.2$, 0.3 and 0.35 (top to bottom respectively). The yield surface is shown as a dashed line and the plug regions are shaded. The bottom plots correspond to the solution given by *Tallarico and Dragoni* [2000] reproduced in Figure 3.

[73] In order to find the solution $\mathbf{f}(\mathbf{x}) = \mathbf{0}$ using a quasi-Newton method, we require an approximation to the inverse of the Jacobian matrix $\mathbf{J} = \partial\mathbf{f}/\partial\mathbf{x}$ (i.e. a matrix $\mathbf{A}$ where $\mathbf{A} \approx \mathbf{J}^{-1}$). Since we don't have an explicit relation between $\mathbf{f}$ and ν and τ_y (which would allow direct calculation of $\mathbf{J}$), we use the two-dimensional flow solution to find an approximate Jacobian $\mathbf{J}_0$. We then use Broyden's method which begins with $\mathbf{A}_0 = \mathbf{J}_0^{-1}$ and then updates $\mathbf{A}$ at each step based on the value of the cost function $\mathbf{f}$ (see *Press et al.* [1992] for a discussion).

[74] We initialize this algorithm by using the plug width to estimate a starting Bingham number:

$$B_0 = \frac{W_p}{W} B_0^\star$$

where $B^\star$ is given by equation (19). We can then use B_0 and the two dimensional Bingham flow to estimate ν and τ_y, giving $\mathbf{x}_0$ as:

$$\mathbf{x}_0 = \begin{bmatrix} (1 - B_0)^2 g' H^2 / 2U_m \\ \rho g' H B_0 \end{bmatrix}. \tag{27}$$

[75] We also use B_0 and the two dimensional Bingham flow to derive an initial approximation to the Jacobian (given in Appendix B):

$$\mathbf{J}_0 = \begin{bmatrix} \dfrac{2U_m}{g' H^2 (1 - B_0)^2} & \dfrac{2}{\rho g' H (1 - B_0)} \\ 0 & \dfrac{1}{\rho g' H B^\star} \left(\dfrac{W}{W - W_p} \right) \end{bmatrix} \tag{28}$$

and set $\mathbf{A}_0 = \mathbf{J}_0^{-1}$.

[76] Then for $n \geq 0$, given $\mathbf{x}_n$ and $\mathbf{A}_n$, we iterate the following procedure:

[77] 1. Calculate an update direction:

$$\Delta\mathbf{x}_n = \mathbf{A}_n\mathbf{f}(\mathbf{x}_n).$$

[78] 2. Perform a line search in the direction of $\Delta\mathbf{x}_n$ by:

[79] (i) Calculate an update candidate

$$\mathbf{x}_{n+1} = \mathbf{x}_n + \Delta\mathbf{x}_n.$$

(ii) Check whether any components of $\mathbf{x}_{n+1}$ are invalid (in this case 'valid' means that $\nu > 0$, $\tau_y \geq 0$, and $B \leq B^\star$). If there are invalid components, replace $\Delta\mathbf{x}_n$ by $\Delta\mathbf{x}_n/2$ and repeat these two steps until all components are valid.

If the line search fails to return a valid update candidate after a specified number of iterations, then reset the approximation to the inverse Jacobian, i.e. $\mathbf{A}_n = \mathbf{J}_0^{-1}$ and return to step 1.

[80] 3. Check for convergence; the algorithm has converged if

$$\|\mathbf{f}(\mathbf{x}_{n+1}) - \mathbf{f}(\mathbf{x}_n)\| \leq \delta$$

for some tolerance δ. If the algorithm has converged, the value obtained for $\mathbf{x}$ can then be used to calculate β and B and hence the flow rate Q.

[81] 4. If the convergence test fails, update the approximation to the inverse Jacobian:

$$\mathbf{A}_{n+1} = \mathbf{A}_n + \frac{(\Delta\mathbf{x}_n - \mathbf{A}_n\Delta\mathbf{f}_n)(\Delta\mathbf{x}^{\mathrm{T}}\mathbf{A}_n)}{\Delta\mathbf{x}_n^{\mathrm{T}}\mathbf{A}_n\Delta\mathbf{f}_n}$$

where $\Delta\mathbf{f}_n = \mathbf{f}(\mathbf{x}_{n+1}) - \mathbf{f}(\mathbf{x}_n)$ and $^{\mathrm{T}}$ denotes the vector transpose operator.

[82] 5. Replace n with $n + 1$ and return to step 1.

[83] We note *Tallarico et al.* [2006] suggest the use of two correction factors to estimate bulk rheological parameters and flow rates, one for the walls and one for the Bingham rheology. These correction factors, multiplied together, give an estimate fluid rheology. The use of such methods underestimates the net down-channel flow rate and overestimates the viscosity and yield strength of the lava, especially in the physically interesting cases of low aspect ratios and high Bingham numbers. Furthermore, their method would be very difficult to apply to flows in the field. It assumes that a plug depth is already known, which is problematic because plug depths would be difficult (if not impossible) to measure in the field, and assumption of a plug depth is equivalent to assuming a yield strength. They cannot use a plug width since their correction factor for viscoplastic effects is based on the two dimensional solution (given in section 3.4.1).

[84] This demonstrates that observations of surface velocities, perhaps by analyzing streaks in long-exposure photographs, could give more accurate estimates of bulk lava rheology and flow rates within channeled flows and lava tubes. We suggest that these observations should be made near an erupting vent so as to minimize the effects of solidification on the surface velocity distribution [*Griffiths et al.*, 2003].

6.4. Estimation of Rheology From Flow Rate and Maximum Velocity

[85] Finally we examine the case where we have estimates for the flow rate, maximum velocity and surface plug width, and we require estimates for the flow depth and fluid rheology. Then we have the following problem:

$$\text{Given } Q, U_m \text{ and } W_p, \text{ determine } H, \nu \text{ and } \tau_y.$$

This application is useful in experimental situations [*Griffiths et al.*, 2003].

[86] For this situation we define the unknown vector and cost function as:

$$\mathbf{x} = \begin{bmatrix} H \\ \nu \\ \tau_y \end{bmatrix} \tag{29}$$

and

$$\mathbf{f}(\mathbf{x}) = \begin{bmatrix} 1 - \dfrac{g'H^2}{\nu U_m}\ u_m(\beta, B) \\ 1 - \dfrac{g'H^3W}{\nu Q}\ q(\beta, B) \\ 1 - \dfrac{W}{W - W_p}\left(1 - w_p(\beta, B)\right) \end{bmatrix} \tag{30}$$

respectively, where β and B are evaluated using the current values in $\mathbf{x}$.

[87] To find an initial vector $\mathbf{x}_0$, we take the two-dimensional Newtonian flow as an initial guess at H; using the expressions for the flow rate per unit width and maximum velocity and solving for H, we get:

$$H_0 = \frac{3Q}{2U_mW} \tag{31}$$

[88] We can then use the plug width fraction $w_p = W_p/W$ to estimate the Bingham number:

$$B_0 = w_pB^\star \tag{32}$$

where $B^\star$ is the critical Bingham number given in equation (19) evaluated for $H = H_0$, and then use this Bingham number and maximum velocity to estimate the yield strength and viscosity, giving:

$$\mathbf{x}_0 = \begin{bmatrix} 3Q/2U_mW \\ g'H_0^2(1 - B_0)^2/2U_m \\ \rho g'H_0B_0 \end{bmatrix} \tag{33}$$

for the initial solution vector.

[89] We also require an initial approximation to the Jacobian matrix $\mathbf{J}_0$. As before we use the two-dimensional film-flow limit to approximate q and u_m (details in Appendix B), giving the following expression:

$$\mathbf{J}_0 = \begin{bmatrix} \dfrac{-2}{H_0(1 - B_0)} & \dfrac{2U_m}{g'H_0^2(1 - B_0)^2} & \dfrac{2}{\rho g'H_0(1 - B_0)} \\ \dfrac{-2U_mW}{Q(1 - B_0)} & \dfrac{2U_m^2W(B_0 + 2)}{3g'H_0Q(1 - B_0)^2} & \dfrac{U_mW(1 + B_0)}{\rho g'Q(1 - B_0)} \\ \dfrac{-WB}{(W - W_p)B^\star H_0} & 0 & \dfrac{-W}{\rho g'H_0B^\star(W - W_p)} \end{bmatrix} \tag{34}$$

[90] Armed with the initial vector in equation (33), and the approximation to the Jacobian in equation (34), we can then

Table 1. The Intermediate Results of the Algorithm Described in Section 6.2 to Find the Flow Height for the Calculations Presented in Section 7 Using Field Data From Lava Flows on Mt. Etna[a]

Step (n)	H_n	$\beta(H_n)$	$B(H_n)$	$\|\|f(H_n)\|\|$
0	0.3339	29.95	0.9767	1
1	1.341	7.457	0.2432	0.1277
2	1.488	6.719	0.2191	0.1093
3	1.42	7.04	0.2296	0.002598
4	1.422	7.033	0.2293	6.754e-05

[a]The algorithm takes 4 steps to converge to an accuracy of $\delta = 2 \times 10^{-5}$.

use Broyden's method as outlined in section 6.3 to find the values of H, ν and τ_y for the flow.

7. Example Calculations Using Field Data From Etna

[91] As a demonstration of how to use our numerical results in section 4 and the algorithms in section 6, we consider the dynamics of lava flows erupted by Mt Etna [*Bonaccorso et al.*, 2004]. These lavas typically have a Newtonian rheology at low crystal fractions [*Vona et al.*, 2011], but develop a viscoplastic rheology at moderate crystal fractions [*Chester et al.*, 1985; *Pinkerton and Norton*, 1995]. Here we will use the rheological measurements made by *Pinkerton and Sparks* [1978] on a set of Etnean lava flows erupted in 1975 (the emplacement of these flows is described by *Pinkerton and Sparks* [1976]). This flow had an internal temperature of 1086 ± 3°C, a modal crystal fraction of 0.45–0.47, a measured yield strength of $\tau_y = 370 \pm 30$ Pa, and a yielded fluid viscosity of $\mu = 9400 \pm 1500$ Pa s. The Etna lava flows in 1975 contained $15 \pm 5\%$ vesicles by volume [*Pinkerton and Sparks*, 1976]. With a non-vesicular lava density of 2600 kg m^{-3} this gives a density of 2210 ± 130 kg m^{-3} and a kinematic viscosity of $\nu = 4.25 \pm 0.68$ m^2 s^{-1} for the vesicular lava.

[92] We consider a channeled flow starting near the summit of Mt Etna, with a width of 5 m and a slope of 10° (similar to the geometries for the 1975 eruption specified by *Pinkerton and Sparks* [1976]). Since the flow is under air, $\rho_a = 0$ and the effective downstream gravitational acceleration is $g' = 1.704$ m s^{-2} for a vertical gravitational acceleration of $g = 9.81$ m s^{-2}. Using equation (24), we can calculate the minimum flow depth for a flow of this yield strength and width: $H^\star = 9.3 \pm 0.7$ cm. If the source feeding our flow were to cease erupting, this depth would represent the remaining thickness of the flow once it had drained, provided the rheological properties of the lava did not change dramatically.

[93] We assume that the flow has a depth of 1 m. This flow has a (prescribed) aspect ratio of $\beta = 5$, and a Bingham number of $B = 0.098 \pm 0.008$. Using the results in Figures 8, 9, 10, and 11, such a flow would have flow rate of $Q = 0.411 \pm 0.005$ m^3 s^{-1}, a maximum velocity of $U_m = 0.147 \pm 0.002$ m s^{-1}, a central plug surface width of $W_p = 1.05 \pm 0.04$ m and a plug depth of $H_p = 13.8 \pm 0.7$ cm. These measured velocities and flow rates agree well with the values given by *Pinkerton and Sparks* [1976].

[94] Suppose that the flow reaches the lower slopes of Mt Etna, where the inclination of the ground surface is 3°, so that the flow widens to $W = 10$ m but continues to flow at the same flow rate, while the rheological properties remain constant. Using equation (24), the minimum depth of this flow is $H^\star = 33 \pm 2$ cm, and using the algorithm in section 6.1, we can solve for the depth of this flow, giving $H = 1.422 \pm 0.007$ m (the results of each iteration in the algorithm are shown in Table 1). This depth means the flow has an aspect ratio of $\beta = 7.03 \pm 0.03$ and a Bingham number of $B = 0.22 \pm 0.02$. Using β and B, and the results in Figures 9, 10, and 11, we see that the maximum velocity of this flow would be $U_m = 0.064 \pm 0.002$ m s^{-1}, with a central plug surface plug depth of $H_p = 56 \pm 2$ cm and a width of $W_p = 4.29 \pm 0.15$ m.

[95] Finally, as an example of the algorithm outlined in section 6.3, we return to the original flow near the vent ($W = 5$, $H = 1$, $\theta = 10°$) and use the maximum velocity and surface plug width obtained there to determine the fluid rheology. The results of each iteration of the algorithm are shown in Table 2, and the final result gives us a yielded fluid viscosity of $\nu = 4.2 \pm 0.8$ m^2 s^{-1} and a yield strength of $\tau_y = 370 \pm 37$ Pa, in good agreement with our original values.

8. Conclusions

[96] In this study we have analyzed the channeled flow of an isothermal Bingham lava using a multigrid-based augmented Lagrangian method. This method converges to known analytical values in the limiting cases of two dimensional flow and Newtonian fluid rheology. We have also highlighted and explained flaws within the models of *Johnson* [1970], *Tallarico and Dragoni* [2000], and *Tallarico et al.* [2006].

[97] Our numerical results show that an internal viscoplastic rheology significantly modifies the surface velocity distribution of a lava flow through the development of plug regions, even when the yield strength is small. At low Bingham numbers the plug regions are small. However, with an increasing Bingham number the plugs grow larger until flow ceases everywhere in the channel at some critical Bingham number. These plug regions (1) thicken the flow and (2) remove shear strain from the center of the flow surface. Plugs also form in the corners of the channel and have a concave shape.

[98] The presence of a yield strength in a high aspect ratio flow generates a significant unyielded region at the flow surface. The width of this central plug region W_p is relatively insensitive to variations in yield strength at moderate to high Bingham numbers. This is because the significant zones of surface shear are restricted to regions with a width of order H near the walls, so that at high aspect ratio $W_p \sim W - 2H$.

Table 2. The Intermediate Results of the Algorithm Described in Section 6.3 to Find the Fluid Rheology for the Calculations Presented in Section 7[a]

Step (n)	τ_{y_n}	ν_n	$\beta(\mathbf{x}_n)$	$B(\mathbf{x}_n)$	$\|\|f(\mathbf{x}_n)\|\|$
0	2.032	1435	10	0.3813	0.4527
1	2.819	818.5	10	0.2174	0.1758
2	3.681	491	10	0.1304	0.07266
3	4.032	402	10	0.1068	0.03362
4	4.166	381.2	10	0.1013	0.01369
5	4.245	370	10	0.09828	0.002083
6	4.249	370	10	0.09828	0.001085
7	4.253	370	10	0.09828	2.268e-06
8	4.253	370	10	0.09828	2.398e-09

[a]The algorithm takes 8 steps to converge to an accuracy of $\delta = 2 \times 10^{-5}$. The results from the line searches in Step 2 are not shown.

At low Bingham number the central plug region is extremely thin, and it may be altered by irregularities in the channel geometry such as bends and changes in slope.

[99] In section 6 we described several algorithms which extend our calculations to situations where some of the parameters on which either the aspect ratio or Bingham number depend are unknown. These methods converge reasonably quickly and are useful for a number of field situations. Field geologists will be particularly interested in the case where the flow rate, fluid viscosity and yield strength can be accurately estimated from measurements of the flow depth, maximum downstream velocity and central plug width at the flow surface. The results of the numerical code are provided as a comma-delimited file in the auxiliary material for this paper.[1] All of the code written for this study (both the multigrid solver used to obtain the numerical flow solutions, written in C++, and implementations of the algorithms in section 6, written in Python) can be made available by contacting the first author.

[100] Finally, we end by noting that changes in temperature play an important role in determining the dynamics of viscoplastic lava flows, since the interactions between convection, solidification and rheology are not trivial [*Griffiths*, 2000; *Griffiths et al.*, 2003; *Cashman et al.*, 2006]. For example the presence of a plug on the flow surface will increase the stability of the surface crust, modifying the feedbacks between cooling, solidification and insulation of the flow. As another example, the lack of advection in the two corner plug regions will mean that they will cool and solidify, changing the shape of the channel. We aim to examine the non-isothermal features of viscoplastic lava flow dynamics in more detail in a future paper.

Appendix A: Calculating Critical Yield Strengths

[101] As discussed in the introduction, the size of plug regions is dependent on the yield strength of the fluid, with higher yield strengths corresponding to larger plugs. To find the size of the yield strength required to stop the channel flow, we can consider the special limiting case immediately before the central and corner plugs meet. In this instance, the yielded layer in the flow shrinks to a line: the limiting yield surface. The yield strength corresponding to this limiting yield surface is $\tau_y^\star$. This appendix outlines how to obtain the critical yield strengths ($\tau_y^\star$) given in section 3.4, which has been provided by *Mosolov and Mjasnikov* [1965, 1966, 1967] as part of their study of the variational form of the problem in equation (5).

[102] To begin, define Ω as the channel cross-section (in dimensional terms), so that

$$\Omega = \left\{ (y,z) : -\frac{W}{2} \le y \le \frac{W}{2},\ 0 \le z \le H \right\}.$$

[103] Consider the set of all possible central plug regions ω which are subregions of Ω. As a useful metric of plug size, define ξ as the ratio of the size of a given central plug region ω to the length of the yield surface that defines its boundary (denoted $\partial\omega$), i.e.:

$$\xi(\omega) = \frac{\text{area}(\omega)}{\text{length}(\partial\omega)}. \tag{A1}$$

[1]Auxiliary materials are available at ftp://ftp.agu.org/apend/jb/2011JB008550.

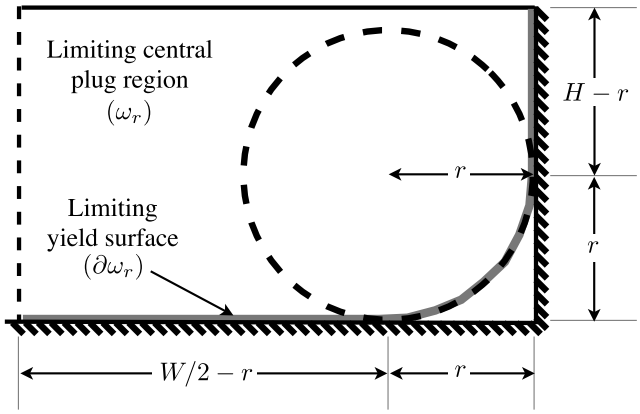

Figure A1. Determining the geometry of the critical central plug $\omega^\star$; we generate possible central plug regions ω_r with yield surfaces described by the channel walls and a circle of radius r. Then we select $\omega^\star$ as the ω_r with r which maximizes the central plug area to yield surface ratio ξ. Walls are shown as hatched lines, the flow centerline by the dashed line on the left and the yield surfaces in grey.

[104] Theorem 1 of *Mosolov and Mjasnikov* [1965] shows that the critical central plug region $\omega^\star$ satisfies $\xi(\omega^\star) \ge \xi(\omega)$ for all $\omega \in \Omega$, while Lemma 2.4 shows that $\xi(\omega^\star)$ is a function of $\tau_y^\star$:

$$\xi(\omega^\star) = \frac{\tau_y^\star}{\rho g' }. \tag{A2}$$

[105] Thus if we find $\xi(\omega^\star)$, we can easily determine $\tau_y^\star$. We also recover a critical Bingham number $B^\star$ corresponding to this yield strength as follows:

$$B^\star = \frac{\tau_y^\star}{\rho g' H} = \frac{\xi(\omega^\star)}{H}. \tag{A3}$$

[106] Lemma 2.3 of *Mosolov and Mjasnikov* [1965] shows that any portion of the boundary of $\omega^\star$ which is not part of the channel boundary will form a circular arc which is tangential to the channel boundary at either end. Therefore we need only consider the set of plug shapes $\omega_r \subseteq \Omega$ that result from replacing the corners of the rectangular domain by circles of radius r, as shown in Figure A1. By calculating the boundary and area of such a domain, we can then see that for these plugs

$$\xi(\omega_r) = \frac{2WH + (\pi - 4)r^2}{2W + 4H + 2(\pi - 4)r}$$

for $0 < r \le \min(H, W/2)$.

[107] A straightforward calculation shows that the maximum of ξ over ω_r is

$$\xi(\omega^\star) = \frac{W + 2H - \sqrt{4H^2 + W^2 - (2\pi - 4)WH}}{4 - \pi}.$$

[108] Using this expression and either equation (A2) or equation (A3) it is straightforward to recover the expressions

for the critical Bingham number $B^\star$ and aspect ratio $\beta^\star$ given in the body of the paper.

Appendix B: Estimating Jacobians for Sections 6.3 and 6.4

[109] In section 6.3, we provided expressions for initial approximations to the Jacobian J of the cost function $\mathbf{f}(\mathbf{x})$. We have three different components which go into the cost function:

$$f_1 = 1 - \frac{g'H^2}{\nu U_m}\, u_m(\beta, B)$$
$$f_2 = 1 - \frac{g'H^3 W}{\nu Q}\, q(\beta, B)$$
$$f_3 = 1 - \frac{W}{W - W_p}\big(1 - w_p(\beta, B)\big).$$

The problem in section 6.3 is simply that for section 6.4 without H as an unknown, and with the removal of f_2 from the cost function. Therefore we treat the calculation of the Jacobian for section 6.4, and the Jacobian for section 6.3 is found by removing the relevant components dependent on f_2 or $\partial/\partial H$.

[110] To derive the Jacobian we use approximations to w_p, q and u_m. In the first we approximate the dependence of w_p on B by a linear function between $B = 0$ and $B = B^\star$, so that

$$w_p \approx \frac{B_0}{B^\star}.$$

Secondly we approximate the maximum velocity and flow rate by those for the two dimensional Bingham flow, given in equations (13) and (14), with $B = B_0$ and $H = H_0$.

[111] By substituting these expressions into $\mathbf{f}$ we can obtain derivatives with which to estimate the components of the Jacobian. The derivatives for f_1 are:

$$\frac{\partial f_1}{\partial H} \approx -\frac{2}{H_0(1 - B_0)},$$
$$\frac{\partial f_1}{\partial \nu} \approx \frac{2U_m}{g'H^2(1 - B_0)^2},$$
$$\frac{\partial f_1}{\partial \tau_y} \approx \frac{2}{\rho g' H(1 - B_0)};$$

the derivatives for f_2 are:

$$\frac{\partial f_2}{\partial H} \approx -\frac{2U_m W}{Q(1 - B_0)},$$
$$\frac{\partial f_2}{\partial \nu} \approx \frac{2U_m^2 W(2 + B_0)}{3g'H_0 Q(1 - B_0)^2},$$
$$\frac{\partial f_2}{\partial \tau_y} \approx \frac{U_m W(1 + B_0)}{\rho g' Q(1 - B_0)};$$

and the derivatives for f_3 are:

$$\frac{\partial f_3}{\partial H} \approx -\frac{WB}{(W - W_p)B^\star H_0}$$
$$\frac{\partial f_3}{\partial \nu} \approx 0$$
$$\frac{\partial f_3}{\partial \tau_y} \approx \frac{W}{\rho g' H B^\star (W - W_p)}$$

from which we have the expression for $\mathbf{J}_0$ given in equations (28) or (34).

Notation

- $\mathbf{A}$ Approximation to the inverse Jacobian of $\mathbf{f}(\mathbf{x}_n)$.
- B Bingham number.
- $B^\star$ Bingham number at which flow ceases.
- f Cost function, vector cost function, cost function update.
- $\mathbf{f}$ Vector cost function.
- g, g' Gravitational acceleration (prime denotes buoyancy-compensated downslope component), m s^{-2}.
- h_p Plug depth to flow depth ratio.
- H Flow depth, m.
- H_p Central plug depth at flow centerline, m.
- $H^\star$ Minimum flow depth, m.
- $\mathbf{J}$ Jacobian matrix of $\mathbf{f}(\mathbf{x}_n)$.
- n Iteration number (when subscripted refers to the current approximation for parameter).
- q Dimensionless down-channel flow rate per unit width.
- Q Total down-channel flow rate, m^3 s^{-1}.
- s_n Stress field approximation in augmented Lagrangian algorithm.
- u Dimensionless velocity field.
- u_m Dimensionless maximum surface velocity.
- U Down-channel velocity component field, m s^{-1}.
- U_m Maximum surface velocity, m s^{-1}.
- w_p Central plug width to flow width ratio.
- W Channel width, m.
- W_p Central plug width at flow surface, m.
- $\mathbf{x}$ Solution vector.
- x Dimensionless down-channel coordinate.
- y Dimensionless cross-channel coordinate.
- z Dimensionless coordinate perpendicular to the channel floor.
- α A positive tuning constant for the augmented Lagrangian algorithm.
- β Cross-channel aspect ratio.
- $\beta^\star$ Minimum aspect ratio for a given Bingham number.
- δ Convergence tolerance.
- ε Regularization parameter, s^{-1}.
- $\dot{\epsilon}$ Strain rate tensor, s^{-1}.
- $\dot{\gamma}$ Dimensionless strain rate vector.
- η Apparent viscosity of viscoplastic fluid, Pas.
- λ Lagrange multiplier.
- μ, μ_a Kinematic viscosities of the viscoplastic/ambient fluids, Pas.
- ν Dynamic viscosity of the yielded Bingham fluid, m^{2}s^{-1}.
- ω Central plug region.
- $\omega^\star$ Central plug cross region at the critical yield strength.
- ω_r Regions made by replacing the corners of Ω with circles of radius r.
- Ω Channel cross section.
- ρ, ρ_a Densities of the viscoplastic and ambient fluids, kg m^{-3}.
- τ Stress tensor, Pa.
- τ_y Yield strength, Pa.
- $\tau_y^\star$ Critical yield strength at which flow ceases, Pa.
- θ Channel inclination.

ξ Central plug area to yield surface length ratio, m.
ζ_k Mode number in equations (15)–(17).

[112] **Acknowledgments.** We thank Marshall Ward and Andy Hogg for support and advice throughout the development of the numerical scheme; and Antonio Costa, an anonymous reviewer and an Associate Editor for their constructive reviews. We gratefully acknowledge financial support from ARC grant DP0772770. This study used components of the Blitz++, Boost and netCDF C++ libraries, and the SciPy and NumPy Python libraries — we thank the respective authors for making their code free and open source.

References

Ancey, C. (2007), Plasticity and geophysical flows: A review, *J. Non-Newt. Fluid Mech.*, *142*, 4–35, doi:10.1016/j.jnnfm.2006.05.005.

Bingham, E. C. (1916), An investigation of the laws of plastic flow, *U. S. Bur. Stand. Bull.*, *13*, 309–353.

Bird, R. B., G. C. Dai, and B. J. Yarusso (1983), The rheology and flow of viscoplastic materials, *Rev. Chem. Eng.*, *1*, 1–70.

Bonaccorso, A., S. Calvari, M. Cotelli, C. del Negro, and S. Falsaperla (2004), *Mt. Etna: Volcano Laboratory*, *Geophys. Monogr. Ser.*, vol. 143, AGU, Washington D. C.

Calvari, S., M. Neri, and H. Pinkerton (2002), Effusion rate estimations during the 1999 summit eruption on Mount Etna, and growth of two distinct lava flow fields, *J. Volcanol. Geotherm. Res.*, *119*, 107–123.

Cashman, K. V., R. C. Kerr, and R. W. Griffiths (2006), A laboratory model of surface crust formation and disruption on lava flows through non-uniform channels, *Bull. Volcanol.*, *68*, 753–770, doi:10.1007/s004450050048z.

Chester, D. K., A. M. Duncan, J. E. Guest and C. R. J. Kilburn (1985), *Mt Etna, the Anatomy of a Volcano*, Stanford Univ. Press, Stanford, California

Cimarelli C., A. Costa, S. Mueller, and H. Mader (2011), Rheology of magmas with bimodal crystal size and shape distributions: Insights from analogue experiments, *Geochem. Geophys. Geosyst.*, *12*, Q07024, doi:10.1029/2011GC003606.

Craster, R. V. (1995), Solutions for Herschel-Bulkley flows, *Q. J. Mech. Appl. Math.*, *48*(3), 343–374.

Dean, E. J., R. Glowinski, and G. Guidoboni (2007), On the numerical simulation of Bingham visco-plastic flow: Old and new results, *J. Non-Newt. Fluid Mech.*, *142*, 36–62, doi: 10.1016/j.jnnfm.2006.09.002.

Favalli, M., A. Fornaciai, F. Mazzarini, A. Harris, M. Neri, M. T. Pareschi, S. Tarquini, and E. Boschi (2010), Evolution of an active lava flow field using a multitemporal LIDAR acquisition, *J. Geophys. Res.*, *115*, B11203, doi:10.1029/2010JB007463.

Glowinski, R., and P. Le Tallec (1989), *Augmented Lagrangian and Operator Splitting Methods in Nonlinear Mechanics*, *Stud. Appl. Math.*, vol. 9, Soc. for Ind. and Appl. Math., Philadelphia, Pa.

Gonnermann, H., and M. Manga (2007), The fluid mechanics inside a volcano, *Annu. Rev. Fluid Mech.*, *39*, 321–356.

Griffiths, R. W. (2000), The dynamics of lava flows, *Annu. Rev. Fluid Mech.*, *32*(1), 477–518.

Griffiths, R. W., R. C. Kerr, and K. V. Cashman (2003), Patterns of solidification in channel flows with surface cooling, *J. Fluid Mech.*, *496*, 33–62.

Hoover, S. R., K. V. Cashman, and M. Manga (2001), The yield strength of subliquidus basalts — experimental results, *J. Volcanol. Geotherm. Res.*, *107*, 1–18.

Il'iushin, A. A. (1940), Deformatsiia viazko-plasticheskogo tela (Deformation of a viscous-plastic body), *Uch. zap. MGU, Mekhanika*, *39*, 3–81.

Johnson, A. M. (1970), *Physical Processes in Geology*, Freeman, Cooper, San Francisco, Calif.

Kerr, R. C., and J. R. Lister (1991), The effects of shape on crystal settling and on the rheology of magmas, *J. Geol.*, *99*, 457–467.

Mosolov, P. P., and V. P. Mjasnikov (1965), Variational methods in the theory of the fluidity of a viscous-plastic medium, *J. Mech. Appl. Math.*, *29*, 545–577.

Mosolov, P. P., and V. P. Mjasnikov (1966), On stagnant flow regions of a viscous-plastic medium in pipes, *J. Mech. Appl. Math.*, *30*, 841–854.

Mosolov, P. P., and V. P. Mjasnikov (1967), On qualitative singularities of the flow of a viscous-plastic medium in pipes, *J. Mech. Appl. Math.*, *31*, 609–613.

Oldroyd, J. G. (1947), A rational formulation of the equations of plastic flow for a Bingham solid, *Proc. Camb. Phil. Soc.*, *43*, 100–105.

Papanastasiou, T. C. (1987), Flows of materials with yield stress, *J. Rheol.*, *31*, 385–404.

Pinkerton, H., and G. Norton (1995), Rheological properties of basaltic lavas at sub-liquidus temperatures: Laboratory and field measurements on lavas from Mount Etna, *J. Volcanol. Geotherm. Res. 68*, 307–323.

Pinkerton, H., and R. S. J. Sparks (1976), The 1975 sub-terminal lavas, Mount Etna: A case history of the formation of a compound lava field, *J. Volcanol. Geotherm. Res.*, *1*, 167–182.

Pinkerton, H., and R. S. J. Sparks (1978), Field measurements of the rheology of lava, *Nature*, *276*, 383–385.

Press, W. H., S. A. Teukolsky, W. T. Vetterling, and B. P. Flannery (1992), *Numerical Recipes in C*, 2nd ed., Cambridge Univ. Press, Cambridge, U. K.

Saramito, P., and N. Roquet (2001), An adaptive finite element method for viscoplastic fluid flows in pipes, *Comput. Methods Appl. Mech. Eng.*, *190*, 5391–5412, doi:S00457825(01)00175X.

Tallarico, A., and M. Dragoni (2000), A three-dimensional Bingham model for channeled lava flows, *J. Geophys. Res.*, *105*(B11), 25,969–25,980.

Tallarico, A., M. Dragoni, and G. Zito (2006), Evaluation of lava effusion rate and viscosity from other flow parameters, *J. Geophys. Res.*, *111*, B11205, doi:10.1029/2005JB003762.

Taylor, A. J., and S. D. R. Wilson (1997), Conduit flow of an incompressible, yield-stress fluid, *J. Rheol.*, *4*(1), 93–101.

Vona A., C. Romano, D. B. Dingwell, and D. Giordano (2011), The rheology of crystal-bearing basaltic magmas from Stromboli and Etna, *Geochim. Cosmochim. Acta*, *75*, 3214–3236.

White, F. M. (1990), *Viscous Fluid Flow*, 2nd ed., McGraw-Hill, Boston, Mass.

R. C. Kerr and J. C. Robertson, Research School of Earth Sciences, Australian National University, Canberra, ACT 0200, Australia (jesse.robertson@anu.edu.au).